Submicron Resolution Hyperspectral Quantum Rod Thermal Imaging of Microelectronic Devices

Bahar Öner, James W. Pomeroy and Martin Kuball**

Center for Device Thermography and Reliability, H.H. Wills Physics Lab., University of Bristol, Tyndall Avenue, Bristol, BS8 1TL, United Kingdom

*bahar.oner@bristol.ac.uk, martin.kuball@bristol.ac.uk

KEYWORDS. thermography, quantum rods, hyperspectral imaging, microelectronics, GaN high electron mobility transistor (HEMT).

ABSTRACT. The trend of electronic device miniaturization, from the micro-scale to the nano-scale, presents a temperature measurement challenge. The available techniques have limitations in terms of either resolution, calibration, acquisition time or equipment cost. Here we demonstrate a thermography technique called hyperspectral quantum rod thermal imaging (HQTI), which exploits temperature dependent photoluminescence (PL) emission of quantum rods to obtain the surface temperature map of a biased electronic device, with a straight-forward calibration. This method uses relatively simple, low cost equipment, while achieving submicron spatial resolution. This technique is demonstrated by measuring the thermal map of a direct current (DC) operated Gallium Nitride (GaN) high electron mobility transistor (HEMT), achieving a temperature precision of ~4 ^{o}C, and a ~700-800 nm estimated lateral optical resolution. This is a versatile

method for both measurement in sub-micron scale regions of interest and of larger areas in the hundreds of micrometers range.

INTRODUCTION. Electronic devices continue to be miniaturized and in many cases self-heating occurs in features with a sub-micron length scale[1]. Accurate temperature measurement on this length scale is vital to ensure device performance and reliability. Infrared (IR) thermography has been the most commonly used thermal imaging tool over the last 50 years and is a very useful qualitative failure analysis technique. [2] However, the spatial resolution of all far field optical measurement techniques is diffraction limited to a maximum of ~$\lambda/2$, where λ is the wavelength of the light being analyzed. This is a major restriction for IR thermography which is sensitive in the 3-5 μm wavelength range. Besides, transparency of the substrate results in an underestimation of the actual peak temperature[3], making reliable quantitative temperature assessment difficult.[2-6] Micro-Raman thermography, based on probing temperature dependency of phonon frequencies, was developed as a higher spatial resolution alternative and an 0.5 μm resolution and ±1-10 ºC temperature precision has been demonstrated, depending on the illumination wavelength and material under test, respectively.[7-8]Although this is an established technique in research laboratories, it is a serial point-by-point measurement, requiring long acquisition times to obtain a temperature map. The acquisition times for a single point measurement can vary from seconds to several minutes, depending on the material under test. Microparticle assisted Raman and photoluminescence thermometry along with the scanning thermography have been established to probe surface temperature of microelectronic devices[9-11], while mapping is time consuming due to single point scanning. Recently, transient thermo-reflectance imaging has emerged for wide field temperature measurements.[12-15]Although the technique can provide submicron spatial resolution (0.3-0.5 μm) thermal images with better than a 1 ºC precision, calibrating the thermo-optic coefficient is a challenge for full field imaging of complex multilayer structures. A pixel by pixel calibration of each particular test structure is required, which is time consuming.[15]Scanning

thermal microscopy (SThM) is among the emerging submicron thermal imaging techniques with its high resolution (~100s of nm) below the optical diffraction limit.[16] Whilst it offers high spatial resolution, this is an AFM based technique requiring expertise and expensive equipment. The variable tip-to-surface thermal contact resistance depends on the surface topology and poses a challenge for the quantitative thermal mapping of typical electronic device structures which have trenches and step edges. It also requires special thermal designs of cantilever tips to overcome contact resistance related artefacts.[17] Quantification of the effect of topology on SThM is an active area of research.[16,18-19] Temperature measurement techniques based on fluorescence imaging have also been established[20-23] and recently the fluorescence intensity ratio of a coating material has been used to measure the thermal image of a PCB.[21] Although the technique can be applied to larger structure, the thick fluorescent paint coating obscures accurate temperature measurement at the device level.

Here we demonstrate a new thermography technique, hyperspectral quantum rod thermal imaging (HQTI), benefiting from the light emission of quantum rods (QR), which has a potential to solve these technical challenges by providing submicron spatial resolution surface temperature image with a straightforward one-time calibration procedure. Simple and cost-effective equipment is used, consisting of only a tunable filter and a monochrome camera, combined with QR deposited on the sample under test. We demonstrate the technique on GaN high electron mobility transistor (HEMT) technology, which is the current technology for high speed and high- power applications.[24] High power densities reaching up to tens of W/mm, and temperature gradients of 10's °C/μm, make temperature measurement particularly challenging in this case. To the best of authors` knowledge, this is the first time that hyperspectral imaging of fluorescence of nanoparticles such as QRs has been used to measure the temperature of semiconductor devices

with submicron resolution. Considering the current drive for energy efficient material and devices development, this method is expected to be a useful characterization and failure analysis technique due to its simplicity, cost effectiveness and general applicability.

EXPERIMENTAL DETAILS.

HQTI exploits the temperature dependent emission wavelength of semiconductor nanoparticles, in this case QRs. The nanoparticles are deposited on the surface of the device under test (DUT). Previously, it has been shown that ~1 μm size diamond particles reach thermal equilibrium almost instantaneously with the surface they are in contact with, owing to their low heat capacity and low radiative heat loss, due to their small size.[9] This is also applicable to QRs deposited onto the sample surface. We exploit the temperature dependent peak emission wavelength of QRs. The emission wavelength is measured across the DUT surface through hyperspectral image reconstruction which is converted to a temperature image.

Spectral imaging provides intensity information at a region of interest (ROI) as a three-dimensional (3D) matrix data, i.e. 2D spatial (x,y) and 1D spectral data (λ), namely I (x, y, λ), in a single shot. [25-27] Spectral imaging is classified as multispectral or hyperspectral imaging depending on the number of the spectral data measured, which is a series of images recorded at particular wavelengths. The precise distinction, based on the number of wavelength data points, varies across disciplines.[28,29] Here we use the term hyperspectral imaging as it is widely preferred for the electronics applications. Hyperspectral imaging reduces image acquisition times compared to spectroscopy, which provides only spectral information of a much smaller area at a time, i.e. single point-like measurement I (λ) and requires serial mapping for image acquisition. We

combined the wide field of view feature of the hyperspectral imaging with the highly efficient QR emitters to probe surface temperature of the DUT, on which they are deposited.

QRs are semiconductor nanoparticles typically with 1-100 nm length and 1-10 nm diameter; the band gap can be varied with their size due to quantum confinement effects. QRs (or alternatively, quantum dots, which are the spherical counterparts of QRs with 2-10 nm diameter) with a 450-620 nm maximum emission wavelength range, have been used commercially in the display industry, e.g., in liquid crystal display (LCD) TVs[30], due to their efficient and bright emission. They are ideal optical sensors due to their high quantum efficiency (QE) as well as thermal stability and commercially availability with a narrow size dispersion. The high QE of the QRs (above 60 % for the QRs used in this study) allows for fast and accurate signal detection. QRs are thermally stable up to ~300 ºC (depending on the core morphology as well as synthesis conditions). [31] CdSe/CdS core-shell QRs have been shown to maintain emission stability during over an 800 min test interval at ~140 ºC.[31]

HQTI relies on probing the red shift in peak emission wavelength of QRs with increasing temperature. The QR excitation wavelength is selected to be above the band gap of the QR but below the band gap of the materials within the DUT, ensuring that device/material being tested is unaffected by photocurrent or direct optical heating during the temperature measurement. We selected CdSe/CdS quantum rods (StremDots™ Series A Plus, size: dia.3-5 nm x length 15-20 nm with 560±8 nm emission wavelength), as they are one of the most efficient commercially available QR light emitters, with a QE of ~ %60. Their high emission efficiency aids signal detection, ultimately increasing signal to noise ratio (SNR) in the temperature measurement. Other alternative fluorescent nanoparticles, such as N-V nanodiamonds[32], carbon dots, metal nanoparticles[33] or

heavy metal-free quantum dots[34] could also be utilized depending on the specific application and the material system under test.

After the QRs have been deposited onto the surface of the DUT (See Methods), they are excited under continuous illumination and the images at each emission wavelength is obtained by sweeping a tunable liquid crystal filter (Thorlabs, Kurious-WB1/M ^{TM} , 420-730 nm) with a predefined wavelength interval (See Methods) such that the QR emission spectrum is fully covered, images of which are successively captured by a 16-bit monochrome camera (See Figure S1 for the emission images). This eliminates the need for a spectrometer and we shall demonstrate that the hyperspectral imaging concept can be extended to thermal imaging. The schematic of the experimental set-up is illustrated in Figure 1. The built system has a ~600 nm diffraction limited theoretical resolution (d), using the Sparrow criterion $d=0.47\,\lambda\,/NA$ where λ is the peak emission wavelength (approximately ~600 nm over the measured temperature range) and NA is the numerical aperture of the objective lens used. The measured optical spatial resolution is ~680 ±20 nm, which is only ~12% lower than the theoretical resolution limit (See Figure S3 and Methods). The pixel resolution in our optical set-up corresponds to ~180 nm, i.e. spatially oversampled. The details of the optics used is given in the Methods section.

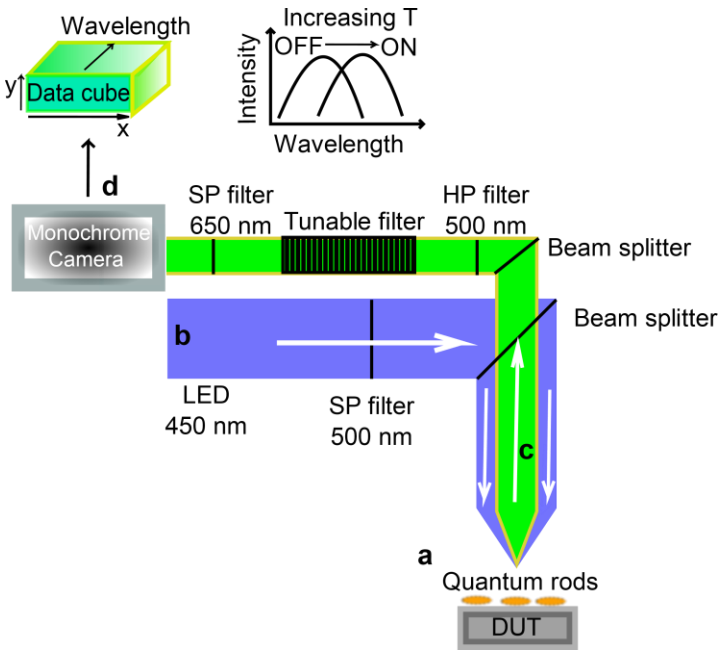

Figure 1. Schematic of quantum rod (QR) thermography set-up. (a) QRs are deposited onto the transistor. (b) A 450 nm LED excites the QRs. (c) QRs photoluminescence is collected. (d) A tunable filter is swept through the emission spectrum and 3D image matrices are captured with a monochrome camera.

RESULTS AND DISCUSSION.

The temperature dependence of the emission wavelength of CdSe/CdS QRs has been previously reported for various QR geometries and sizes.[31] We deposited QRs onto Si (detailed in the Methods section), which was then placed inside a temperature-controlled microscope stage (Linkam THMSG 600) in order to calibrate the temperature response of the QRs in our test set-up, shown in Figure 1. The calibration was performed by changing the stage temperature from 25 °C to 155 °C and the average response over the camera FOV of ~130x175 μm^2 was evaluated (See Methods for the details).

The Varshni equation[35] is a widely used empirical formula, which relates band gap change (or wavelength shift) to temperature. At temperatures above ~200 K, the Varshni equation produces a linear relationship between the wavelength shift and temperature. Fig. 2a shows that the peak emission wavelength shift with respect to the temperature change is non-linear when measured using our test set-up. This is attributed to the QR emission being convoluted with the spectral response of the optical measurement system; for example, the tunable liquid crystal filter transmission and camera sensitivity are wavelength dependent. The actual QR emission spectrum could be obtained by deconvoluting the measured spectrum, although we preferred to fit the data with a quadratic function, including the system response in the calibration for the sake of computational simplicity. The calibrated emission wavelength temperature dependence is ~1.15 nm shift per 10 ^{o}C at ambient temperature, where the fitting was assumed to be for simplicity a quadratic function $\lambda_{cw}=\alpha T+\beta T^2$,where $\alpha=0.072\pm0.0036$ nm/^{o}C, $\beta=3.48\text{x}10^{-4}$ ±4.21 x 10^{-5} nm/(^{o}C)^2. Figure 2a illustrates that the measured QR emission wavelength temperature dependency is similar to reported values for small (2.2 nm) and medium sized (3.8x3.6 nm) QR cores up to 100 ^{o}C.[31] A slight discrepancy is observed between the measured and reported wavelength shift at higher temperatures, which is attributed to the response of the optical measurement system described previously. This is a one-off calibration.

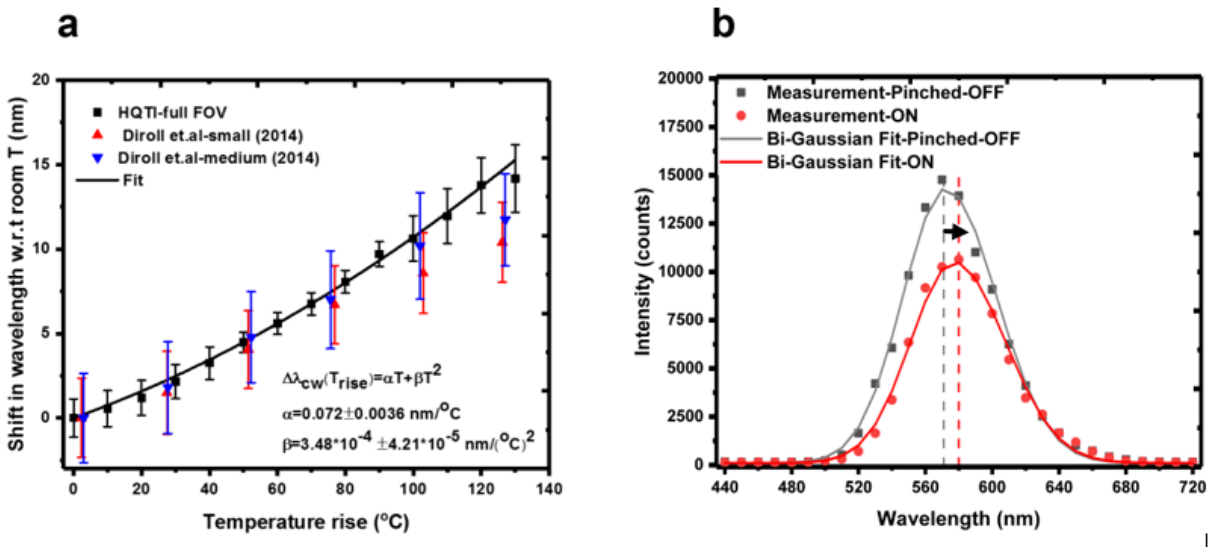

Figure 2. (a) Temperature calibration of QRs deposited on a silicon wafer and an example spectrum taken at a single pixel. Centre photoluminescence wavelength of the QRs as function of temperature is fitted with a second order polynomial function, having a ~1.15 nm shift per 10 ºC at the ambient temperature. Ref[31] data for small and medium sized QRs (Reproduced from [DIROLL, B. T. ; MURRAY, C. B. HIGH TEMPERATURE PHOTOLUMINESCENCE OF CDSE/CDS CORE/SHELL NANOHETEROSTRUCTURES, *ACS NANO*, **2014** ,8, 6466–6474.] Copyright [2014] American Chemical Society) is overlaid for comparison. (b) A sample photoluminescence spectrum and bi-Gaussian fit taken at a single pixel of a 2x2 binned image in the middle of the channel of the DUT with QR deposited upon. The arrow indicates the red shift in center wavelength between the pinched-OFF (reference) and ON state due to the device heating.

In order to demonstrate HQTI, a normally-OFF GaN device on a Si substrate [37], passivated with a Si_xN_y and SiO_2 layer, was tested. The details of the device geometry are given in the Methods section. A schematic cross section of the device and optical white light image is shown

in Figure 3a and Figure 3b, respectively. Once the calibration is performed, peak positions at the ON and pinched-OFF (reference) states of the DUT can be related to temperature of the quantum rods by using the calibration function shown in Figure 2a. Figure 2b illustrates emission curves for the ON and pinched-OFF state of a GaN HEMT, along with the emission peak center fitting function. The emission spectrum follows a bi-Gaussian shape due to a combination of factors, such as small size variations of nanoparticles, thermal broadening and measurement system response. Figure 2b shows an example of the bi-Gaussian function fitted to a pixel spectrum to determine the peak emission wavelength. A least squares iterative algorithm results in fits with an R-squared value >0.95, for spectra with an adequate signal/noise ratio. The fitting routine is described in more detail in the Methods section. The spectra shown in Figure 2b follow the expected trend, i.e., increasing emission wavelength and decreasing intensity, as the temperature rises.[36]

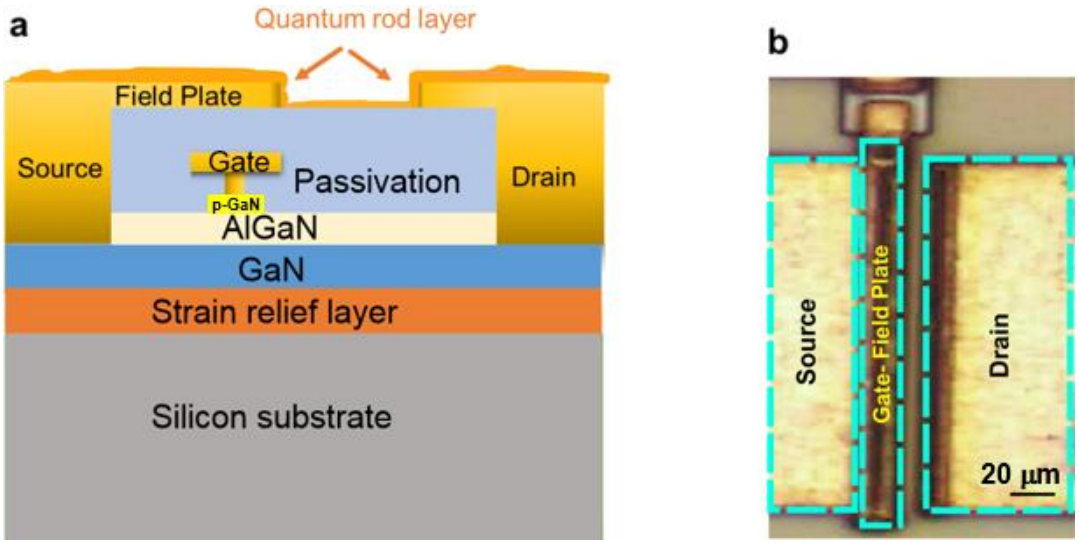

Figure 3. Details of the device under test. (a) Schematic cross section of the GaN on Si HEMT (not to scale). Quantum rods are deposited on the surface, covering the metal contacts and the passivation layer. (b) White light optical image of the device under test.

The normally-OFF single finger GaN HEMT shown in Figure 3 (measured on wafer), was fixed on a thermoelectric vacuum chuck and tested at three different bias conditions to demonstrate the technique. The chuck temperature was set to 25 ºC and the total power dissipation was varied from 0 to 0.83 W, by changing drain bias at a constant gate bias of V_{gs}=5V (I_{gs}=0.01A). The pinch-off condition was used as a reference measurement, by applying V_{gs}=0 V at the same drain bias with the ON state, so that no drain current flows and the device is at the ambient chuck temperature.[38] At these surface electric field levels, the unbiased condition can also be used without affecting the measurement accuracy. However, we note that at higher electric fields (>50s kV/cm, depending on the morphology of the nanoparticles), the electro-optic response, known as Quantum Confined Stark Effect (QCSE), can affect the peak position shift. [39-40] In that case, taking the pinched-off state as the reference measurement yields more accurate temperature measurements.

Figure 4a shows a HQTI temperature map (the mean temperature of 7 successive measurements) at P_{diss}=4. 165 W/mm. Qualitatively, the result is as expected: The channel region, where Joule heating is generated, is hotter than the surrounding contacts due to thermal dissipation. The measured HQTI temperature also increases with power dissipation in the expected way (See Figure S4). The estimated precision of the HQTI temperature measurement is ~4 ºC, which is the standard error of the mean of 7 temperature acquisitions (See Methods for the details). The single thermal map data acquisition takes ~1 min with the proof-of-the-concept set-up, which can be improved further with a higher power excitation source (while ensuring not to cause excessive heating) and a higher quantum efficient detector. Image processing for a single measurement takes ~15 min on an Intel i7 3.10 GHz processor, which can also be enhanced by implementing parallel processing algorithms.

Our measurement revealed a fairly uniform temperature distribution (no hotspots and a small temperature gradient) in the device channel. In order to verify our finding, we performed an infrared (IR) thermography (Quantum Focus Instruments (QFI) InfraScope) measurement on the same device and at the maximum power dissipation used for the HQTI measurements. The chuck temperature was set to 52 ^{o}C for the IR thermography measurements to achieve higher SNR by increasing the thermal radiation according to Planck`s law. The drain bias was increased to compensate for the drain current reduction at the higher ambient temperature (V_{ds}=11.3 V, I_{ds}=73.8 mA, V_{gs}=5V, I_{gs}=0.01 A). A 15x, 0.5NA lens was used for IR thermography measurements. The details of the equipment used and its resolution limits are discussed in detail in Ref.[3] (See also Methods). IR thermography also confirmed there are no hotspots within the channel by revealing a uniform temperature distribution in the channel opening between the field plate and the drain contacts. Even though IR thermography is useful for a qualitative comparison (such as a quick assessment of hot spots present), IR measurements need to be interpreted carefully. IR thermography underestimates temperature rise compared to HQTI in the active region of the device by up to~50% because of lateral (IR wavelength diffraction limit) and axial (semiconductor IR transparency) spatial averaging, which is discussed extensively in Refs.[3-5].

In order to validate the temperature distributions measured using HQTI, we simulated the device thermal behavior using finite element method (FEM). The thermal conductivity of the strain relief layer (SRL) and Si substrate are dependent on processing methods and doping, respectively. The thermal conductivity of these layers was obtained by fitting a thermal simulation to Raman thermography measurements of ungated (TLM) structures on the same wafer (See Methods). Established values were used for the other materials (See details in the Methods section). The temperature rise occurs due to Joule heating ($\mathbf{J}\cdot\mathbf{E}$) in the 2DEG channel formed on the GaN side

of AlGaN and GaN layers. A simplified 3 nm thick uniform heat source is used in the model to represent Joule heating between the source and drain opening, approximating the channel as a simple resistor.[41] Further details about the model are given in Methods section (See also Figure S5). The simulated surface temperature of the device shown in Figure 4b reproduces the peak temperature and main features seen in the HQTI thermal image as shown in Figure 5a, with a maximum deviation of ~8ºC from the measured value. Also overlaid is the simulated channel temperature at the AlGaN/GaN interface showing a somewhat wider distribution, illustrating the impact the source connected field plate and gate contact has on local heat flow.

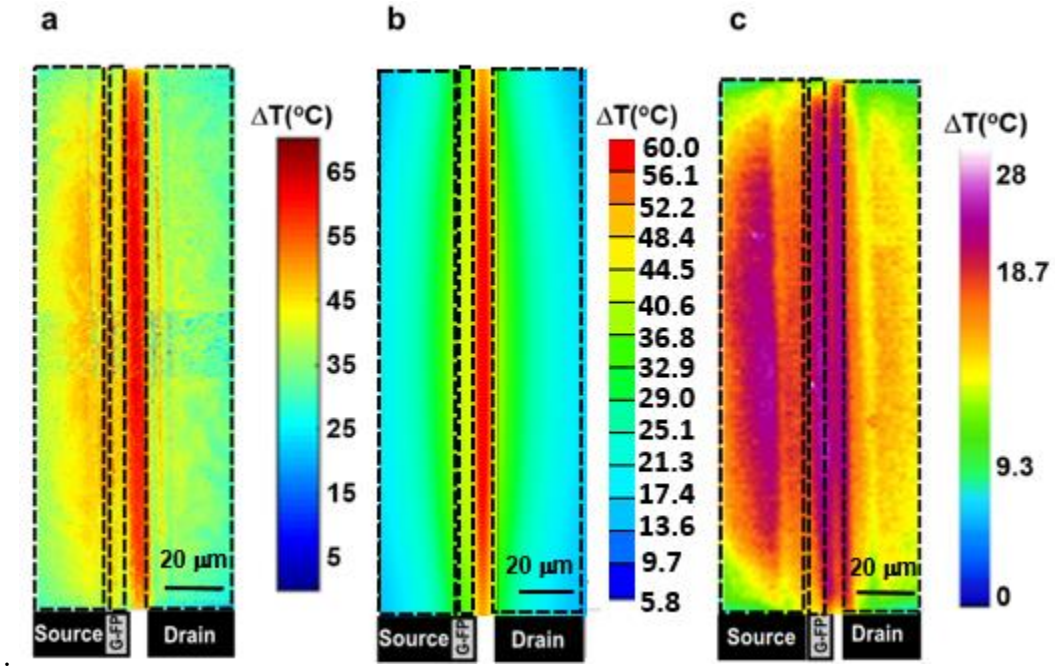

Figure 4. Temperature rise (ΔT) map of GaN single finger device on Si substrate: (a) HQTI image under V_{ds}=10 V, I_{ds}=83.2 mA, V_{gs}=5 V, P_{diss}=4.165 W/mm W,$T_{\text{back plate}}$=25ºC. As the channel width is larger than the FOV, the full image was acquired in three successive acquisitions and patched into a single image (See Figure S4 for a single image). The measured temperature is

equivalent to peak surface temperature of the device, i.e., in this case at the surface of passivation layer and metal contacts. (b) Thermal finite element modeling results. (c) IR thermography image at the same power dissipation in (a), with $T_{back\ plate}$=52 ºC and V_{ds}=11.3 V, I_{ds}=73.8 mA.

The thermal simulation predicts that the channel is hotter than the contacts, as expected, which is also observed in the HQTI temperature line as shown in Figure 5a. In contrast, the temperature profile measured by lower spatial resolution IR thermography in the same region is flat. This demonstrates the submicron optical spatial resolution and the high sensitivity of HQTI, benefiting from the use of QR for temperature measurements, to detect such fine features which are currently not easily accessible using other present thermography techniques.

Thermal resistance (temperature rise divided by power density) is an important parameter for the thermal reliability benchmarking of microelectronic devices. Figure 5b illustrates that estimating thermal resistance based on IR thermography measurements results in an ~0.4× underestimation, which might lead to insufficient thermal management during the design stage and eventually early failure if the effect of depth and lateral averaging in the experimental results are not taken into account. This illustrates the advantage of HQTI over IR thermal imaging in the sense that HQTI provides both large area mapping and accurate surface temperature probing. The lateral spatial resolution of HQTI is further much higher (~700 nm, illustrated here with 50x, 0.5NA) than the fundamental limit of IR imaging spatial resolution, ~3-5 μm.

The hotter source metal revealed both by HQTI and IR measurements indicates that the joule heating distribution is skewed toward the source. The uniform channel heating approximation used in the model produces a reasonable agreement with the measured HQTI surface temperature distribution (Fig. 5a), within 5°C of the peak temperature value. At higher bias voltages, >10V V_{ds}

Joule heating is concentrated within an 0.5μm-long region at the drain edge of the gate.[41] However, using that Joule heating distribution in the thermal simulation produces a poor fit to the HQTI temperature measurement close to the channel, as illustrated in Fig.S5d, although does reproduce the measured increased source metal temperature shown in Fig.S5c-d. The HQTI measurement shows that the actual temperature distribution is somewhere between these two extremes, highlighting the importance of high spatial resolution temperature measurements for thermal model verification.

To further evaluate the accuracy of HQTI, an identical device on the same wafer was measured using the established Raman nanoparticle thermometry technique.[42,43] Raman nano-thermometry also has a submicron spatial resolution and is therefore a suitable reference to confirm the validity of HQTI measured temperatures. The surface temperature is probed through temperature dependent shift of TiO_2 nanoparticles deposited on the surface (See Methods for the description of the Raman thermography measurements); the measurement location is therefore equivalent to HQTI. Temperatures measured by Raman nanoparticle thermometry match the HQTI temperature and the thermal simulation results at the center of the DUT, within the experimental precision, as shown in Figure 5b. This correlation also confirms that the QR deposition has no measurable effect on the DUT surface temperature or thermal resistance (See Methods and Figure S14 for the details). However, QR layer might have an observable effect when deposited on a very low thermal conductivity material system, which should be considered when applying this technique.

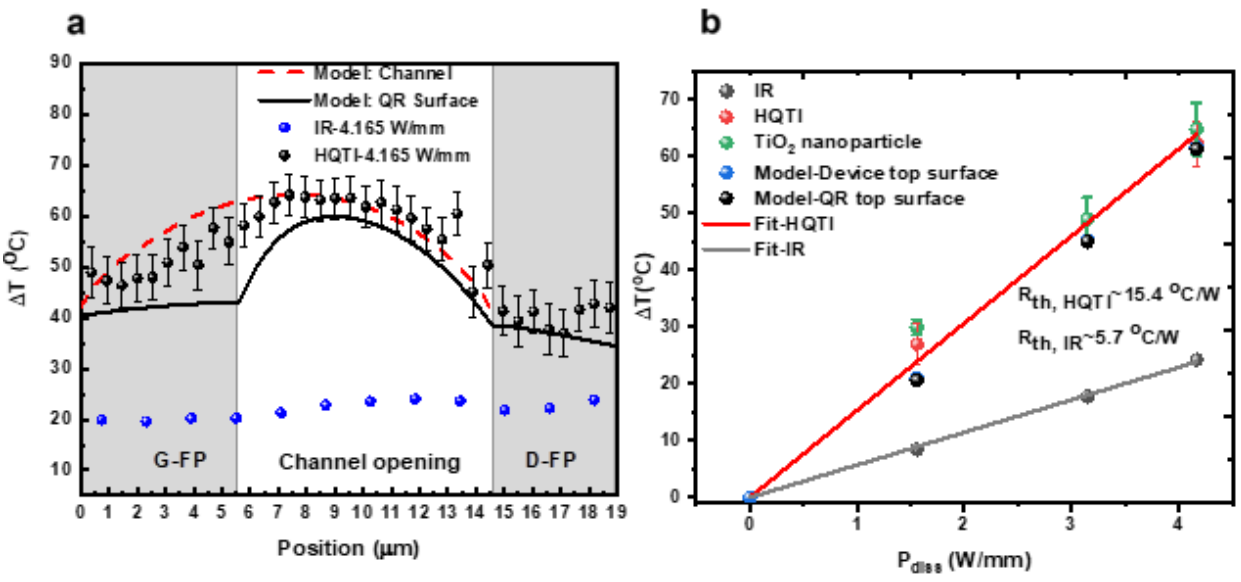

Figure 5. (a) Temperature rise (ΔT) in single-finger GaN on Si substrate device, determined using HQTI, from source connected field plate metal to drain metal. The HQTI data represents a lateral temperature average over its diffraction limited optical resolution (~700 nm). Overlaid is the results of a thermal finite element model, with the temperature shown on the device top surface and within the device channel at the AlGaN/GaN interface. (b) Maximum surface temperature rise vs power dissipation for the thermal resistance estimation of the device, determined using HQTI. TiO_2 nanoparticle Raman thermometry and IR thermography at the peak temperature location in the device. Also displayed are the results of the thermal finite element model.

The theoretical optical resolution limit of our test set-up is ~600 nm, considering the peak emission wavelength reaching up to ~600 nm at high temperatures, while the experimental optical resolution is estimated as ~680±20 nm, which can be conservatively approximated as ~700-800 nm during the actual operating conditions (See Methods for details.). Yet, the resolution of the system can be easily increased using a higher NA lens or solid immersion lenses and a higher band gap (corresponding to shorter peak emission wavelength) quantum rods or quantum dots. As an

alternative to hardware solutions, numerical resolution enhancement techniques, such as, but not limited to[44]super resolution translation microscopy (TRAM)[45], can be adopted depending on the requirements of the application.

CONCLUSION. We developed a surface sensitive and generic sub-micron resolution, wide field thermal imaging technique with a simple data analysis and device independent one-off calibration approach. We introduced nanoparticle assisted hyperspectral thermography approach for the first time by exploiting temperature dependence of quantum rod emission. We illustrated the advantage of the new technique over standard IR thermography on a DC operated device, exhibiting high spatial resolution and surface sensitivity. We verified the accuracy of HQTI by using the well-established Raman nanoparticle thermometry technique. Finite element thermal simulations were shown to support our measurement results. HQTI is a generic and flexible technique and its application is not limited to the material systems tested here. The straightforward one-off calibration procedure of HQTI is advantageous when mapping complex structures, compared to time-consuming pixel-by-pixel calibration such as in IR thermography or thermo-reflectance. HQTI uses low cost, off-the-shelf components, and has a potential applications in testing new device designs or for reliability assessment, e.g., for accurate life time estimation of microelectronics and improved thermal management.

METHODS.

QR deposition on GaN transistor. Commercial CdSe/CdS quantum rods (QR) (StremDots™ Series A Plus, size: dia.3-5 nm x length 15-20 nm) with the peak emission range (560 ± 8 nm) were used. The supplied QR's were suspended in hexane, with a concentration of 5mg/ml. QRs were then diluted to ~1.5 mg/ml and sonicated for one hour in room temperature to prevent

agglomeration of particles and achieve a uniform distribution. The surface of the DUT was treated with Ar plasma (Diener Electronic Zepto) for 1 minute at 0.4 mbar, after standard cleaning with isopropyl alcohol (IPA) and acetone, prior to QR coating, to ensure that we removed any contaminants on the surface of the die. ~10 µl of solvent was drop cast onto the region of interest in the wafer placed on a hot plate heated to 100 ºC, which is above the boiling point of hexane. See Figure S6 for the SEM (Zeiss Sigma VP) image of the QR distribution. A thickness of ~500 nm was measured for the QR layer at the edge of the deposition area using an AFM (Bruker The Dimension Edge) (See Figure S7). This is the thickest (upper limit) region of the deposition where there is a visible accumulation of QRs; the typical layer in the region of interest should be thinner. The effect of QD film thickness on the temperature distribution in the devices is detailed in the thermal simulation of the GaN transistor Methods section. The output and transfer characteristics of the devices was tested before and after the deposition to verify that they do not impact device performance (Figure S8). We performed four terminal measurements to eliminate the errors due to probe contact resistance and the voltage drop across the connection cables. While we did not observe a change in the linear region, we observed a ~0-7 % variation in the output power in the saturation region at some gate biasing conditions (Figure S8a), which is less than the 10% repeatability of the current measurement. This way, we confirmed that HQTI can be applied on passivated devices without significantly affecting device characteristics, for the steady state (under DC biasing) characterization shown here.

HQTI equipment and image acquisition settings. The set-up was built using a Leica DMLM microscope. The original microscope light source was replaced by a multi-LED source, with a white light LED (Thorlabs MWWHL4), for viewing the sample, and blue LED (Thorlabs M450LP1, 450±20 nm, 1850 mW), as the excitation source for photoluminescence from the QRs

(See Figure S9 for LED spectra), mounted perpendicular to each other, with light being directed by a dichroic mirror (Thorlabs DMLP490R) with a 490 nm cut-on wavelength. The blue LED optical power reaching the sample surface is ~25 mW, within an illumination spot of ~1 mm in diameter. The camera (Thorlabs CS2100-M USB 3.0) field of view is ~130x175 μm with a Leica infinity corrected, 50x, 0.5NA objective lens, corresponding to a light power flux of 0.032 W/mm^2 on the sample. Considering the worst-case scenario, assuming that all of the incident power is absorbed by the QR layer and not reflected or scattered, optical heating of the surface would be less than ~0.01 W/mm^2 (considering that QE of QRs is 60%). Including this additional source, an upper limit of less than ~1 ^{o}C temperature rise is predicted using thermal simulations, which is negligible. In reality, a large proportion of the incident light is either reflected from the metal or transmitted through transparent regions, reducing the optical heating.

A 500 nm cut-off short-pass filter (Thorlabs FESH0500) was placed between the blue LED and the sample to block light originating from LED in the QR emission range. A further 500 nm high-pass filter (Thorlabs FELH0500) was placed between the DUT and the tunable filter (Thorlabs KURIOS-VB1/M 420-730 nm) (See Figure S9 for the transmission properties of the bandpass setting used) to block the blue LED light reflecting off the surface of the DUT. Electroluminescence (EL) from the devices can occur at high electric field and high current, which might interfere with the PL emission of QRs at high biasing conditions in our device system tested (AlGaN/GaN HEMT). We placed a 650 nm short pass filter (Thorlabs FES0650) in front of the detector to eliminate this signal as the dominant EL emission is in the near infrared region for the devices under test.[46]

Photoluminescence emission curves from the QRs were obtained by sweeping the liquid crystal tunable filter from 440 to 720 nm with a 10 nm step. The filter has three different bandwidth

setting options, namely, wide, medium and narrow. We used the wide setting of 25-40 nm bandwidth (depending on central wavelength) which has the highest transmission, improving SNR (See Figure S9 for the transmission properties of the bandpass setting used). A 10 nm step size was selected following Nyquist-Shannon sampling theorem to avoid undersampling[47]. A 16-bit, 1040x1392 pixel, monochrome camera (Thorlabs CS2100-M USB 3.0) was used to detect emission from the field of view at each measurement wavelength. In order to improve SNR and reduce computational burden for image reconstruction, the images were binned in 2x2 CCD pixels using MATLAB built-in image resizing function, i.e. imresize, and image size reduced to 520x696 pixels. The pixel resolution using this configuration for the measurement was then ~180 nm.

System calibration was performed by depositing QRs onto a silicon wafer, which was mounted in a cryostat (Linkam TMS600). The QR emission wavelength was measured by averaging the full FOV (See Figure S10 for the emission images of the calibration sample.) over a range of temperatures. We also verified that the temperature dependent emission wavelength shift is uniform across various ROIs, defined at the edge, center and side of the FOV (See Figure S11), which justifies the average FOV calibration approach.

Image drift due to thermal expansion of the DUT is important to consider for accurate submicron level optical temperature measurements as it potentially leads to erroneous temperature estimations. In order to correct for the focal plane change due to the axial drift and the lateral drift due to thermal expansion, especially during the calibration process, the sample position was automatically corrected in the XY and Z directions using a computer controlled XYZ stage with 100nm step precision and an in-house developed LabVIEW software. This procedure was run each time after the hot stage temperature was changed, during the calibration. The focal plane correction software finds the focal plane by moving the sample stage in the Z direction to the height where

the image intensity is the highest. The XY drift is corrected to within 1 pixel by moving the stage to minimize the difference between a white light illuminated live image and a reference image previously recorded, using an image registration method.[48] We note that the sample drift was only found to be significant during the calibration, as the heated volume in the hot stage is much larger than that of the actual measured device during operation, which is mounted on a thermal vacuum chuck at a fixed temperature. Focus shift was not observed during actual device temperature measurements. A representative example of the effect of the XY drift correction by image registration on the calibration data is shown in Figure S2. As an additional confirmation, images at the ON and pinched-OFF state were overlaid on ImageJ software before temperature image reconstruction, to ensure that sample image does not drift between ON and pinched-OFF state due to thermal expansion. The image correction with 1 pixel accuracy for the raw image (no binning) corresponds to 90 nm accuracy. During the measurement, the device drifts at the pixel level. Conservatively, the temperature image spatial resolution is 700-800 nm, accounting for sample drift due to thermal expansion.

Line spread function (LSF) estimation of the imaging system for the determination of the experimental lateral spatial resolution. We measured the LSF of our imaging system using the well-known knife edge method.[49] A sample, with a sharp discontinuity from a reflective (metal coated) area to a transmissive area, was imaged under white light illumination. AFM scan (Figure S3a) shows that this sample approximates a step function, with a transition on a length scale much less than the measurement wavelength. The liquid crystal tunable filter was set to the maximum emission wavelength of the quantum rods (560 nm). The measured response (Figure S3a.) is the convolution of the LSF and the actual object (which can be approximated as a step function as shown in Figure S3a), which can be mathematically expressed as[50]:

$$g(X) = \int_{-\infty}^{\infty} f(x)h(X-x)dx \qquad (1)$$

where *g(X)* is the measured reflectivity (the convoluted response), *f(x)* is the real object, i.e. actual line profile, and *h(X-x)* is the line spread function (LSF).

Naturally, when *f(x)* is a step function, the derivative of measured reflectivity (the expression above), gives the LSF profile as shown in Figure S3a. The full width at the half maximum (FWHM) of the Gaussian function fitted to LSF with 0.94 R-square value, is 680 ± 20 nm. The measured optical resolution is therefore within ~12% of the theoretical estimate of 600 nm.

Statistics used in image processing. We eliminated pixels having an intensity below 500 counts, considering the background noise (~350 counts for the longest camera exposure time of 7765 ms used at room temperature), to ensure that we process the actual QR emission signal (See Figure S1 for the emission intensity distribution). Hot pixels were eliminated by applying a 95% maximum intensity threshold. The resulting data was fitted with a bi-Gaussian function, implemented with the built-in nonlinear curve fitting function in LabVIEW, which utilizes the Levenberg-Marquardt bounded algorithm for optimization. We defined the tolerance of the fit, which is the mean squared difference between the measured spectrum and the nonlinear fit, as a user defined parameter and decreased the tolerance until numerical temperature convergence is achieved. For the results presented here, this value was 10^{-2}. The goodness of the fit was verified by applying Chi-squared test to the fitted values using a built-in LabVIEW function Goodness of fit.vi, showing that R-square value is greater than 0.95. Further data processing was performed by eliminating any spurious peak position detected outside of the swept spectrum range, 440-720 nm in our case. This procedure was applied to 7 measurements (images) for each ON and reference pinched-OFF state measured. The outliers in successive measurements were removed by applying

mean of absolute deviation (MAD) criteria as discussed in Ref.[51]. The outliers are assigned a zero peak position and are attributed to random noise in the measurement system. If the peak position (center wavelength) is non-zero for both ON and pinched-OFF state at a particular pixel, then temperature was calculated using the predetermined calibration function. Otherwise the pixel temperature is assigned as not-a-number (NaN). The image processing algorithm chart is given in Figure S12. The precision of the temperature measurement was quantified by calculating the standard error of the sample mean temperature (sample being 7 successive measurements) for each pixel which was not rejected. We note that the precision is highly dependent on the fitting accuracy, which increases with the SNR. We define SNR as the peak emission intensity divided by the baseline intensity. As can be inferred from the emission images in Figure S1, the minimum SNR for the case presented in Figure 4 is ~22, which is high enough to recover the temperature map shown in Figure 4a. We note that the SNR scales with the square root of the acquisition time, i.e. $SNR\ \alpha\ \sqrt{t}$.

Test measurements were performed at $T_{baseplate}$=25ºC with no device heating (OFF at V_{ds}=10 V, I_{ds}=0 mA). A histogram of the distribution of the sample mean temperature estimations over the whole image size (for n=3 measurements) around the 25°C ambient temperature is shown in Figure S13, resulting in 20±8 ºC estimated population mean temperature. This analysis further increases the confidence in the temperature estimations, as the estimation covers the set temperature of 25°C. A more comprehensive discussion of the error analysis is given in Supplementary Information.

IR thermography equipment and image acquisition settings. The infrared (IR) thermal imaging equipment described in Ref.[3,5] was used in this study, i.e. Quantum Focus Instrument (QFI) Infrascope, integrated into a Leica DMLM microscope, with LN_2 cooled 256x256 InSb detector.

A 16 mm working distance SiGe 15x 0.5 NA objective lens was used. The resulting total field of view is ~410 x410 μm with 1.6 μm pixel resolution. The chuck temperature was set to 52ºC to increase the device IR emission above the ambient thermal radiation.

TiO_2 nanoparticle Raman thermography measurement. The Raman nanoparticle thermometry technique described in Ref.[42,43] was applied to probe the surface temperature of an identical device for the verification of HQTI measurements. A 99.98% purity suspension with 30 nm diameter TiO_2 particles was sonicated and then drop casted onto the surface of the device. The lowest frequency E_g mode (~143 cm^{-1})[42,43] was measured to determine the temperature of the particles. A 532 nm laser with a 50x 0.5NA Leica infinity corrected objective lens was used, resulting in a focused spot size of 0.5 μm on the sample surface. The temperature calibration function determined in our previous work[42] was used. The particle in the middle of the channel opening between the field plate metal and the drain contact and 41 μm along the gate width was selected due to its high Raman scattering intensity. As the particles are small, they do not affect the device thermal resistance.[9] Four measurements were performed at each P_{diss}. The error is within ±5ºC. The Si temperature, which represents the average of the ~1 μm probing depth with 532 nm laser, was also measured simultaneously in the same Raman spectra and used as an additional reference point for the thermal model. The Si temperature was also measured 225 μm away the edge of the active device, where there is negligible heat flux. The thermal resistance between the chuck and the wafer was adjusted in the thermal model to match the temperature rise measured at this location. More information about the Raman thermometry method can be found in Ref.[7].

Thermal property determination using a TLM structure, through Raman thermography measurement and thermal FEM simulation. The thermal conductivity of the strain relief layer

(SRL) is dependent on the material used and the processing conditions. We have measured the temperature in an ungated device (TLM structure) with 90 μm channel width and 7 μm channel length on the same wafer to estimate the SRL thermal conductivity, using a similar approach as Ref.[52]. TLM structures are ideal for this type of analysis because they generate a uniform heat source between the ohmic contacts and quasi-1D heat flow through the epitaxial layers, into the Si substrate. By measuring the resulting temperature gradient and fitting a thermal model, the thermal conductivity of the SRL and silicon substrate can be determined. 488 nm Ar^+ laser with 50x0.5 NA Leica infinity corrected objective lens was used for this measurement. A power dissipation of 0.494 W was applied to the TLM and the chuck temperature fixed at 25°C. The GaN temperature was determined from E_2 phonon mode shift[53]. GaN is transparent at this wavelength and the measured temperature is a volumetric the average through the GaN layer. A ΔT_{max} of ~70 ºC was generated between the GaN layer and Si temperature, which allowed the estimation of the SRL thermal conductivity in between the GaN and the Si substrate. The estimated effective thermal conductivity of SRL was 24 W/mK, which is comparable to the reported values in the literature. [53] A Si thermal conductivity of 134 W/mK with $(T/300)^{-1.3}$ was also obtained from this analysis, within the range of reported literature values. [39,54]

Thermal simulation of GaN transistor. Commercial FEM software ANSYS was used for the steady state thermal simulation. We considered one half of the device in the simulation, taking advantage of its mirror symmetry. (See Figure S5 for the model overview). The model includes the single-finger AlGaN/GaN device with an 80 nm thick AlGaN barrier grown on top of GaN layer with a total thickness of 0.75 μm, and a 3.7 μm-thick strain relief layer on 700 μm thick Si substrate. The T-shape gate and the field-plate are considered, along with the device passivation with an 800 nm-thick Si_xN_y and SiO_2 layer. The device under test is 200 μm-wide, having 1.8 μm

source-gate and 12 μm gate-drain distance. The gate foot to field plate edge distance is 3 μm. A 3 nm thick volumetric heater is placed between the source and the drain contact, in GaN layer, at the AlGaN/GaN interface[41], representing device heating within the 2DEG conduction channel. We note that as the bias conditions are in the knee region (See Figure S8b), it is expected that the heating profile would be slightly more concentrated between the gate-drain region. [41]. The actual channel heating profile will be a combination of resistive heating in the access region and at the gate edge, which may only be quantified with a detailed drift-diffusion electrothermal simulation. However, for low voltage levels as in this work, it is a fair assumption to consider a uniform heating profile within the channel width[55]. The thermal contact resistance between the wafer and the aluminum chuck was adjusted to $5x10^{11}$ W/m^{2}K, matching the temperature measured by Raman thermography 225 μm away from the device. Thermal conductivities of metal contacts (gold), AlGaN, GaN and passivation were set as 310 W/m·K, 25 W/m·K [41], 160 W/m·K[53], and 1.1 W/m·K,[41] with a $(300/T)^{1.4}$ temperature dependency for GaN. [3,41]. The thermal conductivities obtained from the TLM measurements were used for the Si and SRL layers. The Fourier heat equation was solved with a 25ºC isothermal boundary condition at the chuck back side, all other boundary conditions are set as insulating. Convection and radiation heat transfer effects are negligible because of the small heated area. The validity of this assumption was confirmed by comparing the simulated temperature with and without radiative/convective heat transfer boundaries, resulting in less than 0.01 ºC temperature change, even when assuming an emissivity of 1 and h_{conv}=20 W/m^{2}K for all the surfaces. The meshing was refined until the solution was mesh independent, and relative error in the calculated heat flux was of the order of 10^{-5}. The surface temperature was extracted from the simulation for a direct comparison with the HQTI measurements. The model was used to assess the effect of the QR layer on the measured

temperature. Assuming a thermal conductivity of k=4.9 W/mK [56] for the QR layer and a 500 nm deposition thickness (upper limit) results in ~ 0.1 ^{o}C ΔT between the passivation surface and top of the QR layer, as shown in Figure S14. The main impact of QR layer thickness variation on the measurements is a reduction in accuracy when the QR layer is too sparse, caused by a reduction in the signal-to-noise ratio.

Supporting Information. The following files are available free of charge. PL emission images of the DUT and the calibration sample; Image correction effect on the calibration data; Optical resolution measurement; Verification of HQTI technique with the increasing P_{diss}; Details of the thermal FEM model; SEM image of the QR deposited DUT; AFM image of the QR deposited DUT and the film thickness measurement; The details of the built optical system; Verification of the full FOV calibration approach; Image processing algorithm chart and its verification; The effect of QR layer on the electrical and thermal performance of DUT; Error analysis (PDF)

Corresponding Author

*bahar.oner@bristol.ac.uk, martin.kuball@bristol.ac.uk.

Author Contributions

B.Ö. designed and performed the feasibility study, conducted the experiments and simulations, developed the thermal image reconstruction algorithm, analyzed the data and generated the figures.

J.W.P. and M.K. set the project goals and managed the project. J.W.P. envisioned the initial concept and provided significant input and expertise on the interpretation of the data and on the technical aspects. B.Ö. wrote the manuscript with the assistance from J.W.P. and M.K. All authors contributed to the discussion of the results and reviewed the manuscript.

Funding Sources

This work was partially funded by the Engineering and Physical Sciences Research Council (EPSRC) under Program Grant GaN-DaME (EP/P00945X/1) and by Excellence in Electronics (ECSEL) initiative under grant name PowerBase. The PhD studentship for B.Ö. was financed by Infineon Technologies and University of Bristol Alumni Foundation.

Notes

The authors declare no competing financial interest.

ACKNOWLEDGMENT

The authors thank Infineon Technologies for providing the devices used in this work. B.Ö. acknowledges Infineon Technologies and University of Bristol Alumni Foundation for the studentship and thanks Dr. Ben Rackauskas for his assistance. The authors acknowledge the Engineering and Physical Sciences Research Council (EPSRC) and Excellence in Electronics (ECSEL) initiative for the partial financial support for this work under Program Grant GaN-DaME (EP/P00945X/1) and PowerBase, respectively.

ABBREVIATIONS

HQTI, hyperspectral thermal imaging ; DC, direct current ; QR, quantum rod; HEMT, high electron mobility transistor ; IR, Infrared ; SThM, scanning thermal microscopy, DUT, device

under test; QE, quantum efficiency; LCD, liquid crystal display ; SNR, signal to noise ratio ; FEM, finite element method ; TLM, transmission line method; TRAM, translation microscopy. NA, numerical aperture ; EL, electroluminescence ; SEM, scanning electron microscopy, AFM, atomic force microscopy ; LED, light emitting diode ; FOV, field of view ; LSF, line spread function ; FWHM, full width at half maximum ; MAD, mean of absolute deviation ; SRL, strain relief layer.

REFERENCES

1. Garimella, S. V. ; Fleischer, A. S. ; Murthy, J. Y. ; Keshavarszi, A. ; Prasher, R. ; Patel, C. ; Bhavnani, S. H. ; Venkatasunramanian, R. ; Mahajan, R. ; Joshi, Y. ; Sammakia, B. ; Myers, B. a. ; Chorosinski, L. ; Baelmans, M. ; Sathyamurthy, P. ; Raad, P. E. Thermal Challenges in Next-Generation Electronic Systems. *IEEE Trans. Compon. Packag. Technol.* **2008**, 31, 801-815.

2. Webb, P. W. ,Thermal Imaging of Electronic Devices with Low Surface Emissivity. In *IEE Proceedings G - Circuits, Devices and Systems.* **1991**,138, 390-400.

3. Sarua, A. ; Ji, H. ; Kuball, M. ; Uren, M. J. ; Martin, T. ; Hilton, K. ; Balmer, R. Integrated micro-Raman/Infrared thermography Probe for Monitoring Self-Heating in AlGaN/GaN Transistor Structures. *IEEE Transactions on Electron Devices.* **2006**, 53, 2438-2447.

4. Blackburn, D. L. A Review of Thermal Characterisation of Power Transistors. *In Proceedings of Semiconductor Thermal and Temperature Measurement Symposium*, San Diego, CA, **1988**.

5. Killat, N. ; Kuball, M. ; Chou, T. M. ; Chowdhury, U. ; Jimenez, J. Temperature Assessment of AlGaN/GaN HEMTs: A Comparative Study by Raman, Electrical and IR Thermography. *In Reliability Physics Symposium (IRPS)*. Anaheim, CA, **2010**.

6. Oxley, C. H. ; R. H. Hopper. Effect of Transparency within a Semiconductor on Emissivity Mapping for Thermal Profile Measurements of a Semiconductor Device, *IET Sci.Meas.Technol.*, **2007**, 1, 79-81.

7. Kuball, M. ; Hayes, J. M. ; Uren, M. J. ; Martin, T. ; Birbeck, J. C. ; Balmer, R. S. ; Hughes, B. T. Measurement of Temperature in Active High-Power AlGaN/GaN HFETs Using Raman Spectroscopy, *IEEE Electron Device Lett.* **2002**, 23, 7-9.

8. Pomeroy, J. W. ; Kuball, M . A Review of Raman Thermography for Electronic and Opto-Electronic Device, *IEEE Trans. Device and Mater. Reliaby.* **2016**, 16, 667-684.

9. Simon, R. B. ; Pomeroy, J. ; Kuball, M. Diamond Micro-Raman Thermometers For Accurate Gate Temperature Measurements. *Appl. Phys. Lett.* **2014**, 104, 213503-1-213503-4.

10. Gu, P. ; Zhang, Y. ; Feng, Y. ; Zhang, T. ; Chu, H. ; Cui, T. ; Wang, Y. ; Zhao, J. ;. Yu, W. W . Real-Time and On-Chip Surface Temperature Sensing of GaN LED Chips Using PbSe Quantum Dots. *Nanoscale*, **2013**, 5, 10481–10486.

11. Aigouy, L. ; Tessier, G. Scanning Thermal Imaging of Microelectronic Circuits with a Flourescent Probe. *Appl.Phys.Lett.* **2005**, 87, 184105-1-184105-3.

12. Cahill, D. G. ; Goodson, K. ; Majumdar, A. . Thermometry and Thermal Transport in Micro/Nanoscale Solid-State Devices and Structures. *J.Heat Transfer*. **2002**, 124, 223-241.

13. Christofferson, J.; Shakouri, A. Thermoreflectance Based Thermal Microscope. *Rev. Sci. Instrum.* **2005**, 76, 024903-1-024903-6.

14. Maize, K. ; Ziabari, A. ; French, W. D. ; Lindorfer, P. ; OConnell, B. ; Shakouri, A. Thermoreflectance CCD Imaging of Self-Heating in Power MOSFET Arrays. *IEEE Trans. Electron Devices.* **2014** , 61, 3014-3053.

15. Kendig, D. ; Yazawa, K. ; Shakouri, A. Hyperspectral Thermoreflectance Imaging for Power Devices, I*n IEEE 33rd SEMI-THERM Symposium*, San Jose, CA, USA, **2017**.

16. Gomes, S. ; Assy, A. ; Chapuis, P.O. Scanning Thermal Microscopy: A Review, *Phys.Status Solidi A.* **2015**, 212, 477-494.

17. Shi, L. : Plyasunov,S. ; Bachtold, A. ; McEuen, P.L. ; Majumdar, A. Scanning Thermal Microscopy of Carbon Nanotubes Using Batch-Fabricated Probes. *Appl.Phys.Lett.* **2000**, 77, 4295-4297.

18. Bodzenta, J. ; Juszczyk, J. ; Kazmierczak-Balata, A. ; Firek, P. ; Fleming, A. ; Chirtoc, M. Quantitative Thermal Microscopy Measurement with Thermal Probe Driven by dc+ac Current, *Int. J Thermophy.* **2016**, 37:73.

19. Tovee, P. ; Pumarol, M. ; Zeze, D. ; Kjoller, K. ; Kolosov, O. Nanoscale Spatial Resolution Probes for Scanning Thermal Microscopy. *Journal of Applied Physics.* **2012**, 112, 114317-1-114317-11.

20. J. C. Waters, Accuracy and Precision in Quantitative Flourescence Microscopy. *J.Cell Bio.***2009**, 185, 1135-1148.

21. Chin, P. T. ; Buckle, T. ; Miguel, A. A. de ; Meskers, S. C. ; Janssen, R. A. ; Leeuwen, F. W. Dual-Emissive Quantum Dots for Multispectral Intraoperative Flourescence Imaging. *Biomaterials.* **2010**, 31, 6823-6832.

22. Xiong, J. ; Zhao, M. ; Han, X. ; Cao, Z. ; Wei, X. ; Chen, Y. ; Duan, C. ; Yin, M. Real-Time Micro-Scale Temperature Imaging at Low Cost Based on Flourescent Intensity Ratio. *Sci. Rep.* **2017**, 7, 41311-1-41311-8.

23. Brites, C. D. ; Lima, P. P. ; Silva, N. J. ; Millan, A. ; Amaral, V. S. ; Palacio, F. ; Carlos, L. D. Thermometry at the Nanoscale. *Nanoscale.* **2012**, 4, 4799-4829.

24. Palacios, T. ; Chakraborty, A. ; Rajan, S. ; Poblenz, C. ; Keller, S. ; DenBaars, S. P. ; Speck, J. S. ; Mishra, U. K. High-power AlGaN/GaN HEMTs for Ka-band Applications, *IEEE Electron Device Lett*, **2005**, 26, 781-783.

25. Garini, Y. ; Young, I. T. ; McNamara, G. Spectral Imaging: Principles and Applications. *Cytometry A*. **2006**, 69, 735–747.

26. Prats-Montalban, J. M. ,; Juan , A. ; Ferrer, A. Multivariate image analysis: A review with applications. *Chemom. Intell. Lab. Syst*. **2011**, 107, 1-23.

27. Edwards, P. R. ; Jagadamma, L. K. ; Bruckbauer, J. ; Liu, C. ; Shields, P. ; Allsopp, D. ; Wang, T. ; Martin, R. W. High-Resolution Cathodoluminescence Hyperspectral Imaging of Nitride Nanostructures. *Micros.Microanal.* **2002**, 18, 1212-1219.

28. Mansfield, J. R. Multispectral Imaging : A Review of its Technical Aspects in Anatomic Pathology, *Vet. Pathol.* **2014** ,51, 185-210.

29. Liang, H. Advances in Multispectral and Hyperspectral Imaging for Archaeology and Art Conservation, *Appl. Phys A.* **2012**, 106, 309-323.

30. Shaviv, E. ; Glozman, D. ; Bonfil, Y. ; Banin, U. ; Amir, S. In *SID Digest of Technical Papers*, Semiconductor Quantum Rods for Display Applications. San Jose, CA, **2015,** 71-72.

31. Diroll, B. T. ; Murray, C. B. High Temperature Photoluminescence of CdSe/CdS Core/Shell Nanoheterostructures, *ACS Nano*, **2014** ,8, 6466–6474.

32. Gong, J. ;Steinsultz, N. ; Ouyang, M. Nano Diamond-based Nanostructures for Coupling Nitrogen-Vacancy Centres to Metal Nanoparticles and Semiconductor Quantum Dots. *Nat. Comm.*, **2016**, 7:11820, 1-10.

33. Ng, M. S. ; Koneswaran, M. ; Narayanaswamy, R. A Review on Fluorescent Inorganic Nanoparticles for Optical Sensing Applications. *RSC Adv*, **2016**, 6, 21624–21661.

34. Pickett, N. L.; Harris, J. A. ; Gresty, N. C. In *SID Digest of Technical Papers*, Invited Paper: Heavy Metal-Free Quantum Dots for Display Applications. San Francisco, CA, **2016**, 425-427.

35. Varshni, Y. Temperature Dependence of the Energy Gap in Semiconductors. *Physica*.**1967,** 34, 149-154.

36. Pelton, M. ; Andrews, J. J. ; Fedin, I. ; Talapin, D. V. ; Leng, H. ; O`Leary, S. K. Nonmonotonic Dependence of Auger Recombination Rate on Shell Thickness for CdSe/CdS Core/Shell Nanoplatelets. *Nano Lett.* **2017**, 17, 6900-6906.

37. Amano, H .; Baines, Y.; Beam, E.; Borga, M.; Bouchet, T .; Chalker, P. R.; Charles, M. ; Chen, K.J.; Chowdhury, N.; Chu, R. ; De Santi, C. ; De Souza, M.M. ; Decoutere, S. ; Di Cioccio, L. ; Eckardt, B.; Egawa, R.; Fay, P.; Freedsman, J.J; Guido, L.; Häberlen,O.; Haynes, G.; Heckel, T; Hemakumara, D.; Houston, P.; Hu, J.; Hua, M.; Huang, Q.; Huang, A.; Jiang, S.; Kawai, H.; Kinzer, D.; Kuball, M.; Kumar, A.; Lee, K. B.; Li, X.; Marcon, D.; März, M.; McCarthy, R.; Meneghesso, G.; Meneghini, M.; Morvan, E.; Nakajima, A.; Narayanan, E.M.S; Oliver, S.; Palacios, T.; Piedra, D.; Plissonnier, M.; Reddy, R.; Sun, M.; Thayne, I.; Torres,A.; Trivellin, N.; Unni,V.; Uren, M.J.; Van Hove, M.; Wallis, D.J.; Wang, J.; Xie, J.; Yagi, S.; Yang, S.; Youtsey, C.; Yu, R.; Zanoni, E.; Zeltner, S.; Zhang, Y.The 2018 GaN power electronics roadmap. *J. Phys. D: Appl. Phys.* **2018** , 51, 163001-1-48.

38. Sarua, A. ; Ji, H. ; Kuball, M. Piezoelectric Strain in AlGaN/GaN Heterostructure Field-Effect Transistors Under Bias. *Appl.Phys.Lett.* **2006**, 88, 103502-1-103502-3.

39. Bar-Elli, O.; Steinitz, D.; Yang, G.; Tenne, R. ; Ludwig, A. ; Kuo, Y.; Triller, A.;Weiss, S. ; Oron, D. Rapid Voltage Sensing with Single Nanorods via the Quantum Confined Stark Effect, *ACS Photonics*, **2018** , 7, 2860-2867.

40. Empedocles, S. A.; Bawendi, M. G. Quantum-Confined Stark Effect in Single Cdse Nanocrystallite Quantum Dots, *Science*, **1997**, 278, 2114-2117.

41. Pomeroy, J. W. ; Uren, M. J. ; Lambert, B.; Kuball, M. Operating Channel Temperature in GaN HEMTs: DC versus RF Accelerated Life Testing. *Microelectron. Reliab.* **2015**, 55, 2505-2510.

42. Anaya, J. ; Bai, T. ; Wang, Y. ; Li , C. ; Goorsky, M. ; Bougher T.L.; Yates, L. ; Cheng, Z.; Graham, S. ; Hobart, K.D. ; Feygelson, T.I. ; Tadjer, M.J. ; Anderson, T.J. ; Pate, B.B. ; Kuball, M. Simultaneous determination of the lattice thermal conductivity and grain/grain thermal resistance in polycrystalline diamond. *Acta Mater.* **2017**, 139, 215-225.

43. Dallas, J. ; Pavlidis, G. ; Chatterjee, B. ; Lundh, J. S. ; Ji, M. ; Kim, J. ; Kao, T. ; Detchprohm, T. ; Dupuis, R. D. ; Shen, S. ; Graham, S. ; Choi, S. Thermal Characterization of Gallium Nitride P-I-N Diodes. *Appl. Phys. Lett.***2018**,112, 073503-1- 073503-5.

44. Cremer, C. ; Masters, B. R. Resolution Enhancement Techniques in Microscopy. *Eur. Phys. J. H*. **2013**, 38, 281-344.

45. Qiu, Z. ; Wilson, R. S. ; Liu, Y. ; Dun, A. R. ; Saleeb, R. S. ; Liu, D. ; Rickman, C. ; Frame, M. ; Duncan, R. R. ; Lu, W. Translation Microscopy (TRAM) for Super-Resolution Imaging. *Sci. Rep.* **2016**, 6:19993, 1-10.

446. Brazzini, T. ; Sun, H. ; Sarti, F. ; Pomeroy, J. W. ; Hodges, C. ; Gurioli, M. Vinattieri, ; A. ; Uren, M. J. ; Kuball, M. Mechanism of Hot Electron Electroluminescence in GaN-based Transistors. *J. Phys. D: Appl. Phys.* **2016**, 49, 435101-1-435101-6.

47. Shannon, C.E. Communication in The Presence of Noise (Republished). *Proc. of the IEEE*. **1998** , 86, 447-457.

48. Guizar-Sicairos, M. ; Thurman, T.S.; Fienup J.R. Efficient Subpixel Image Registration Algorithms. *Opt. Lett*. **2008**, 33, 156-158.

49. Reichenbach, S.E.; Park, S.K ; Narayanswamy, R. Characterizing Digital Image Acquisition Devices. *Opt. Eng.* **1991**, 30, 170-177 .

50. Hect, E. *Optics*, Adison Wesley: San Francisco, **2002**.

51. Leys, C. ; Ley, C. ; Klein , O. ; Bernard, P. ; Licata, L. Detecting Outliers: Do Not Use Standard Deviation Around The Mean, Use Absolute Deviation Around The Median. *Journal of Experimental Social Psychology.* **2013,** 49, 764-766.

52. Pomeroy, J.W.; Bernardoni, M.; Dumka, D.C.; Fanning D.M. ; Kuball, M. Low Thermal Resistance GaN-on-Diamond Transistors Characterized by Three Dimensional Raman Thermography Mapping. *Appl. Phys. Lett.* **2014**, 104, 083513-1- 083513-5.

53. Liu, W. ; Balandin, A. A. Temperature Dependence of Thermal Conductivity of Thin Films Measured by 3ω, *Appl. Phys. Lett,* **2004**, 85, 5230-5232.

54. Darwish, A. ; Bayba, A. J. ; Hung, H. A. Channel Temperature Analysis of GaN HEMTs. *IEEE Transactions on Electron Devices.* **2015**, 62, 840-846.

55. Heller, E.; Choi, S.; Dorsey, D.; Vetury, R.; Graham, S. Electrical and Structural Dependence of Operating Temperature of AlGaN/GaN HEMTs. *Microelectron. Reliab.* **2013**, *53*, 872–877.

56. Liu, X. F. ; Wang, R. ; Jiang, Y. P. ; Zhang, Q. ; Shan, X. Y. ; Qiu, X. H.. Thermal Conductivity Measurement of Individual CdS Nanowires Using Microphotoluminescence Spectroscopy. *Journal of Applied Physics.* **2010**, 108, 054310-1-054310-4.

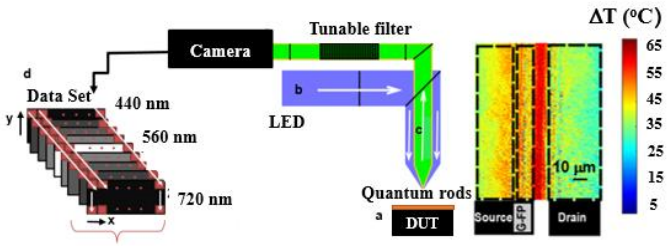

For Table of Contents Only.